PHYSICAL REVIEW B **79**, 174204 (2009)

Metal-insulator transition in Pt-C nanowires grown by focused-ion-beam-induced deposition

A. Fernández-Pacheco,[1,2,3] J. M. De Teresa,[2,3,*] R. Córdoba,[1,3] and M. R. Ibarra[1,2,3]
[1]*Instituto de Nanociencia de Aragón, Universidad de Zaragoza, Zaragoza 50009, Spain*
[2]*Instituto de Ciencia de Materiales de Aragón, Universidad de Zaragoza-CSIC, Facultad de Ciencias, , Zaragoza 50009, Spain*
[3]*Departamento de Física de la Materia Condensada, Facultad de Ciencias, Universidad de Zaragoza, Zaragoza 50009, Spain*
(Received 2 February 2009; published 13 May 2009)

We present a study of the transport properties of Pt-C nanowires created by focused-ion-beam (FIB)-induced deposition. By means of the measurement of the resistance while the deposit is being performed, we observe a progressive decrease in the nanowire resistivity with thickness, changing from 10^8 $\mu\Omega$ cm for thickness $\sim$20 nm to a lowest saturated value of 700 $\mu\Omega$ cm for thickness $>$150 nm. Spectroscopy analysis indicates that this dependence on thickness is caused by a gradient in the metal-carbon ratio as the deposit is grown. We have fabricated nanowires in different ranges of resistivity and studied their conduction mechanism as a function of temperature. A metal-insulator transition as a function of the nanowire thickness is observed. The results will be discussed in terms of the Mott-Anderson theory for noncrystalline materials. An exponential decrease in the conductance with the electric field is found for the most resistive samples, a phenomenon understood by the theory of hopping in lightly doped semiconductors under strong electric fields. This work explains the important discrepancies found in the literature for Pt-C nanostructures grown by FIB and opens the possibility to tune the transport properties of this material by an appropriate selection of the growth parameters.

DOI: 10.1103/PhysRevB.79.174204 PACS number(s): 71.30.+h, 81.07.−b, 81.15.Jj

I. INTRODUCTION

Local deposition by means of focused-ion-beam-induced deposition (FIBID) is an emerging technique to grow nanostructures since it is a highly flexible one-step maskless process with resolution below 50 nm. Because of the important advantages with respect to more conventional nanolithography techniques, FIBID is currently used in a wide range of research applications, as well as in industry.[1,2] The basic principle is simple: a focused ion beam (FIB) is scanned over a surface where a precursor gas is adsorbed. The gas molecules, usually organometallic, contain atoms of the metal to be deposited. From the interaction of the ions with the substrate and the gas molecules, the dissociation of these molecules is produced. The nonvolatile fragment of the molecule remains on the substrate, forming a local deposit where the beam, has been scanned. However, this simple picture is far from reality since a large number of factors play a role in the deposit: interaction volume of the beam with the substrate, mass and penetration depth of ions, energy and mean free path for the generated electrons, ion implantation, thermal diffusion, residual pressure, gas flux, beam overlap, dwell time, ion dose, etc. Therefore, the complete picture is far from being fully understood. Currently, a collision-cascade model is used to give account of the process, with the generated secondary electrons (SEs) being mainly responsible of the deposition.[1,3] For a given precursor molecule, the typical metal content for these deposits is around 30–40 % atomic, the rest being mainly carbon. This percentage is in general much higher than that for the analogous technique where a scanning electron microscope is used [focused electron beam induced deposition (FEBID)] since the gas dissociation process with ions is more effective.[1,4,5] Thus, the main drawback when creating metallic nanostructures with these techniques is the high carbon percentage present in the deposits, which can influence dramatically the properties of these nanostructures. Purification processes after deposition are used to increase the metallic content.[6,7] In the case of FIBID, the damage induced by ions is also an important issue to take into account. For a recent review of the technique see Ref. 1.

One of the most commonly deposited metallic materials using FIBID is Pt. A lot of work has been done regarding its electrical transport properties, with a wide range of reported results on the resistivity at room temperature (ρ_{RT}), as well as on the thermal dependence of the resistance, as pointed out in Ref. 8. We show in Table I the results compiled in that work, together with additional references.[7–18] In addition to the value for ρ_{RT}, we also include, when reported, the thermal coefficient of the resistivity ($\beta = d\rho/dT$), the residual resistivity ratio ($RRR = \rho_{RT}/\rho_{low\ T}$), the electronic mechanism proposed for conduction, the character of current-versus-voltage curves, the chemical composition of the deposits, and the gas precursor used. As revealed by transmission-electron microscopy, the microstructure is found to be inhomogeneous, with crystalline metallic inclusions (around 3–10 nm) embedded in an amorphous carbon (a-C) matrix.[7,9–11,15] An important point that is usually missed when comparing these results is the two types of precursors used for Pt deposition. We can see that in two groups[9–11] and in Ref. 16, the nanowires (NWs) are deposited with cyclopentadienyl-trimethyl platinum, $(CH_3)_3PtCp$, whereas in the rest of groups[7,8,12–15,17,18] methylcyclopentadienyl-trimethyl platinum, $(CH_3)_3Pt(CpCH_3)$ is used. Deposits using the first precursor (one carbon less present in the molecule) have the lowest resistivity reported (only about seven times higher than that of bulk Pt) and a positive β. At low temperatures they present deviations from the behavior expected for pure Pt NWs, such as weak antilocalization and quasi-one-dimensional-interference effects.[9–11] On the contrary, with the second precursor, β is always negative, either

TABLE I. Compilation of reports for Pt-C NWs created by FIB. All deposits are done at 30 kV, except in Ref. 11) (30–40 kV) and Ref. 12) (25 kV). In these two references the atomic percentage is obtained by Auger spectroscopy, whereas the rest are EDX measurements. Contradictory results are found for the transport properties and composition. The present work can explain the differences in terms of a different composition with thickness. In Ref. 8, the nonlinear *I-V* characteristics were observed for a 3078 $\mu\Omega$ cm NW.

Report	ρ_{RT} ($\mu\Omega$ cm)	$\beta=d\rho/dT$	RRR$=\rho_{RT}/\rho_{low\ T}$	Conduction	*I-V* curves	C:Pt:Ga:O at. %	Gas precursor
Lin *et al.*[9–11]	61.5–545	>0	≈ 1.3	Disordered metal	Linear	67:30:3:0	$(CH_3)_3PtCp$
Tao *et al.*[12]	70–700					24:46:28:2	$(CH_3)_3Pt(CpCH_3)$
Puretz *et al.*[13]	400–2100					47:37:13:0	$(CH_3)_3Pt(CpCH_3)$
Telari *et al.*[14]	500–5000					70:20:10:0	$(CH_3)_3Pt(CpCH_3)$
De Teresa *et al.*[15]	800	<0	0.8	Disordered metal	Linear	70:20:10:0	$(CH_3)_3Pt(CpCH_3)$
						Similar to Refs. 12–14	
Peñate-Quesada *et al.*[8]	860–3078	<0	≈ 1	Intergrain tunneling	Nonlinear		$(CH_3)_3Pt(CpCH_3)$
Tsukatani *et al.*[16]	1000	≈ 0	≈ 1				$(CH_3)_3PtCp$
Dovidenko *et al.*[17]	1000–5000					63:31:4:2	$(CH_3)_3Pt(CpCH_3)$
De Marzi *et al.*[18]	2200	<0	≈ 0.7	VRH			$(CH_3)_3Pt(CpCH_3)$
Langford *et al.*[7]	$1000-10^6$	<0	0.6	VRH	Linear	50:45:5:5	$(CH_3)_3Pt(CpCH_3)$
Present study	$700-10^8$	<0	Thickness dependent	MIT	Thickness dependent	Thickness dependent	$(CH_3)_3Pt(CpCH_3)$

with an appreciable thermal dependence, associated with variable-range hopping (VRH),[7,18] or an almost-negligible dependence,[8,15,16] resembling the conduction of a dirty metal, interpreted as metallic[15] or tunneling conduction.[8] In this work, we *center* our study on NWs created with the second precursor, having more extended use in the scientific community, with the aim to clear up, in principle, the contradictory existing results. For it, we employ the same methodology we used in a previous work,[15] with similarities to others,[19–21] where the resistance of the NWs is probed as they are being grown. In this case, by measuring in a four-probe (4W) configuration, we study *in situ* the room-temperature electrical properties of NWs in different ranges of conductivity. The same NWs are studied as a function of temperature. The results are correlated with chemical and microstructural characterizations and can be understood within the framework of the theory by Mott and Davis[22] for disordered materials. The NWs present a metal-insulator transition (MIT) as a function of thickness, with the metal-carbon proportion as the key parameter that determines the type of conduction. We understand the mechanism of conduction for the insulator deposits in terms of Efros-Shklovskii-variable-range hopping.[23] A decrease in the differential conductance with the electric field is observed for the less conductive NWs, which is explained by the trapping of electrons in a lightly doped semiconductor, when hopping under strong electric fields.[24–26] This work tries to unify the previous results found over recent years for Pt-C deposits created by FIB.

II. EXPERIMENTAL DETAILS

A. Deposition parameters

We have grown Pt-C NWs in a commercial dual beam system (Nova 200 Nanolab from FEI), integrating a 30 kV-FIB gallium column and a 30 kV field emission electron column, with an automatic gas injection system (GIS) to introduce the gas into the process chamber. The scanning electron microscopy (SEM) was used for imaging the sample, minimizing the ion dose in the deposits. The deposition parameters are: $(CH_3)_3Pt(CpCH_3)$ precursor gas, $(T_G)=35$ °C precursor temperature, $(V_{FIB})=30$ kV beam voltage, $(I_{FIB})=10$ pA beam current, substrate temperature=22 °C, dwell time=200 ns, chamber base pressure=10^{-6}-10^{-7} mbar, process pressure=3×10^{-6} mbar, beam overlap=0%, and distance between GIS needle and substrate $(L_D)=1.5$ mm. Under these conditions, a dose of 3×10^{16} ion/cm^2-min roughly irradiates the sample. We must emphasize that the values for T_G (about 10 °C below the usual operation temperature) and L_D ($\sim$1.35 mm higher than usually) were chosen to decrease the deposition rate, allowing detailed measurements of the evolution of the resistance as the deposit was realized. This is required to get fine control, especially during the initial stages, where a very abrupt change in the resistance occurs in a very short period of time (see Sec. III C). We obtained approximately the same final resistivity when depositing NWs using normal conditions,[15] so these changes do not seem to affect substantially the properties of the NWs. Thermally oxidized silicon ($\sim$200 nm of SiO_2)

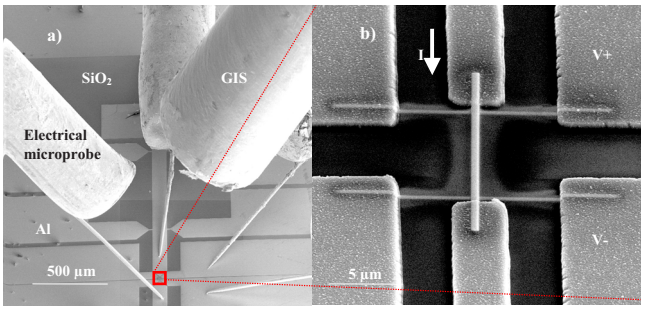

FIG. 1. (Color online) (a) SEM image of the experimental configuration for four-wire electrical measurements. The four microprobes are contacted to Al micrometric pads, while the deposit is carried out. For deposition, the GIS needle is inserted near the substrate. (b) SEM image of one deposited Pt-C NW (top-to-down). The additional two horizontal lines are done before the top-to-down NW, to perform four-wire measurements (see text for details).

was used as substrate, and aluminum pads were previously patterned by optical lithography (see Ref. 15 for details). The studied NWs [top-to-down deposit in Fig. 1(b)] are length $(L)=15$ μm, width $(w)=500$ nm, thickness $(t)=$variable with process time.

B. "In situ" measurements of the resistance during the growth process

The electrical resistance was measured inside the process chamber, using four commercial Kleindiek microprobes, connected via a feedthrough to a 6220 dc current source 2182A nanovoltmeter combined Keithley system. In Fig. 1(a), a SEM image shows the experimental configuration for the deposition, where the four microprobes are contacted to the pads and the GIS needle is inserted near the substrate. By applying a constant current between the two extremes of the NW, and measuring the voltage drop in two of the intermediate pads, we are able to measure the resistance of the NW which is being grown, once it is below 1 GΩ. The probe current (I_{probe}) was changed during the measurement in order to optimize the signal-to-noise ratio and try to minimize heating effects of the device while it was created. Typical values for I_{probe} range from 5 nA at the beginning of the monitoring ($R\sim 1$ GΩ) up to 10 μA at the end ($R\sim 1$ kΩ). All these measurements have been done at room temperature.

In Fig. 1(b) the top-to-down deposit is an example of a studied NW. Before its deposition, additional "perpendicular-to-the-nanowire" deposits were performed (horizontal deposits) for four-wire measurements, avoiding nonlinear effects associated with the resistance of the contacts.[27,28] These extraconnections were done using several growth parameters, finding no differences in the resistance measurements of the NWs. This avoids any influence of the associated halo on the deposition in the results, which could be the source of spurious effects.[17,29]

C. Compositional analysis by EDX

For the study of the composition by energy dispersive X-ray (EDX), we performed deposits on SiO_2 of the same lateral dimensions as those used for electrical measurements and varying thickness. The EDX measurements were done by means of a commercial Oxford INCA 200 EDX setup whose detector is driven in the vicinity of the sample. The selected energy for the microanalysis is 20 kV. Prior to each EDX experiment, energy calibration by means of a Co calibration sample was done.

D. Structural analysis via scanning-transmission electron microscopy

Lamella preparation of selected NWs was performed inside the dual beam equipment by means of Ga ion thinning initially at 30 kV and finally at 5 kV. An Omniprobe nanomanipulator was used to perform *in situ* lift out and placing of the lamella on a Cu grid. The scanning-transmission electron microscopy (STEM) images were obtained inside the same experimental setup, in dark-field mode, under 30 kV and 0.15 nA conditions.

E. XPS measurements

In order to study the chemical nature of the deposits, we have done X-ray photoelectron spectroscopy (XPS) measurements in an axis ultra equipment by Kratos, at a base pressure of 3×10^{-10} Torr. Because of the limited spatial resolution of the X-ray probe, this deposit was much larger in comparison with all the others: length=100 μm$\times$width =100 μm$\times$thickness=200 nm. Under the chosen conditions, previously detailed, this would imply a process time of about 25 h, so we changed the I_{BEAM} to 3 nA, reducing significantly the deposition time. The dose rate, $\sim 10^{16}$ ions/cm^2-min, is approximately the same in both types of experiments. A 5 kV argon etching, with current densities on the order of 0.15 A/m^2 was done to obtain a depth profile of the deposits (probing every 30 nm).

For the quantitative analysis of the XPS spectra, a Shirley-type background was subtracted, using pseudo-Voigt peak profiles with a 10 %–30 % Lorentzian contribution in all edges, except for the Pt 4f. In this case, because of the asymmetry of the peaks, the spectra were analyzed using the Doniach-Sunjic function as follows:[30]

$$I(\varepsilon)=\frac{\Gamma(1-\alpha)}{(\varepsilon^2+\gamma^2)^{(1-\alpha)/2}}\cos\left[\frac{1}{2}\pi\alpha+\theta(\varepsilon)\right], \tag{1a}$$

$$\theta(\varepsilon)=(1+\alpha)\tan^{-1}(\varepsilon/\gamma), \tag{1b}$$

where ε is the energy measured relative to Fermi energy, Γ is the gamma function, γ is the natural linewidth of the hole state corresponding to its lifetime, and α is the line asymmetry parameter. The function was convoluted with a Gaussian curve with FWHM=0.3 eV to take into account the experimental broadening (instrumental resolution, sample inhomogeneity, etc.).[31]

F. Transport measurements as a function of temperature

The measurements of the electrical resistance as a function of temperature were performed in a closed-cycle refrig-

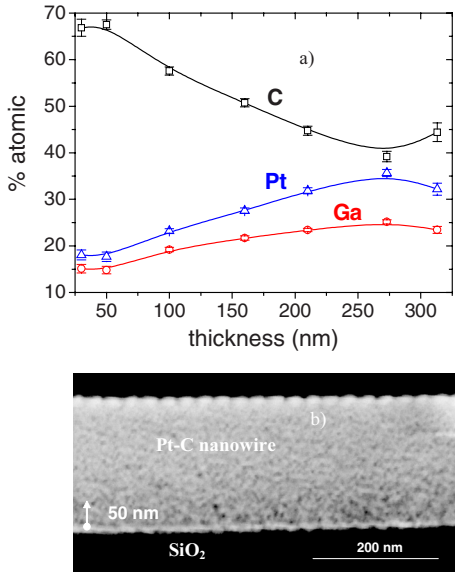

FIG. 2. (Color online) (a) Atomic percentage compositions of Pt-C nanowires as a function of their thickness, determined by EDX. We observe a clear difference in composition for the NWs smaller than 50 nm in comparison with the others, where a higher metallic content is present. Oxygen is always below 1%. (b) STEM dark-field image of a lamella prepared from a 200 nm-thick NW. Approximately, the first deposited 50 nm have a darker contrast in comparison with upper layers, indicating a higher carbon concentration at the initial stages of growth.

erator that allows variation in the temperature from 300 to 25 K by using the Keithley combined system mentioned in Sec. II B.

III. RESULTS

A. Compositional (EDX) and structural (STEM) analysis of the deposits

We performed chemical analysis by EDX on NWs with different thicknesses. The composition was found to be homogeneous over the entire deposited surface. The results are shown in Fig. 2(a). For $t=25$ and 50 nm, the deposit is highly rich in carbon: ~68%, with Pt ~ 18% and Ga ~ 14% (atomic percentages). A residual fraction of oxygen (less than 1%) is also present. For higher thickness, the metal content increases gradually until approximately saturated values: C ~ 40–45%, Pt ~ 30–35%, and Ga ~ 25%.

A lamella has been prepared from a 200-nm-thick NW for STEM imaging inside the chamber. We can see an example in Fig. 2(b), where the difference in dark-bright contrast indicates a gradient in composition as a function of thickness. For the initial deposited nanometers (roughly 50 nm), the image shows a higher C concentration than in the upper part of the deposit, where a higher metal content is present. This agrees perfectly with the former EDX analysis and was previously found in TEM images by Langford *et al.*[7]

We can understand the gradient in composition with thickness taking into account two possible factors. First, an important decrease in the secondary electron yield in SiO_2 that occurs when the SiO_2 is irradiated with ions in the keV range[32] because of the large energy gap present in SiO_2. The SEs are considered to be the main cause of the dissociation of the precursor gas molecules.[1,3] Thus, at the beginning of the growth process, a smaller amount of SE is emitted in comparison with the subsequent stages, when the effective substrate becomes the initial C-Pt-Ga deposit. This thesis is in agreement with the penetration range of Ga at 30 kV in a SiO_2 and Pt-C substrate (on the order of 30–50 nm), as stopping and range of ions in matter (SRIM) calculations indicate.[33] A second explanation can be related to heating effects present during the deposit, which is a crucial point in FIBID and FEBID processes.[1,5,34] As the structure grows in height the heat flow would pass from a three-dimensional regime to a pseudo-two-dimensional regime. Thus, the higher Pt percentage for the top of the structure could be associated with heat dissipation that is less effective than at the beginning of the growth.[1,34] The gradient in metal-carbon concentration with thickness gives rise to a broad phenomenology in the transport properties of the NWs, as will be described later in this work.

B. XPS measurements

In order to gain a more detailed insight into the nature of the FIBID-Pt, we have performed a depth profile XPS analysis in a micrometric sample, which remained in contact with the atmosphere for 1 day after deposition. Survey spectra show the presence of carbon, platinum, gallium, and oxygen, with concentrations similar to those obtained by EDX. A detailed analysis was done by studying the evolution of the absorption edges: C 1*s*, Pt 4*f*, Ga 3*d*, and O 1*s*, as a function of thickness.

(i) Analysis of the C 1*s* edge: the C 1*s* spectra have a constant profile through all the thickness. In Fig. 3(a), we can see the particular case for thickness=170 nm (30 nm ion etched), where four chemical components are used to fit the spectrum. These components are, in order of binding energy: sp^3 carbon with carbon-carbon bonds (C-C sp^3, 283.6 ± 0.1 eV),[35] sp^2 carbon with carbon-carbon bonds (C-C sp^2, 284.3 ± 0.1 eV),[35,36] sp^3 carbon with hydrogen-carbon bonds (C-H sp^3, 285.3 ± 0.1 eV),[35,36] and a C=0 contribution, at 286.2 ± 0.1 eV.[37] This last minor peak is compatible with the O 1*s* spectra (not shown here), where a peak is found at 531.8 ± 0.1 eV. All the peaks have a full width at half maximum of 1.3 ± 0.3 eV.[36] Thus, we find that the carbon present in the deposit has a sp^2 hybridization of around 55%. This percentage is slightly lower than in previous results obtained by energy electron loss spectroscopy in suspended Pt nanostructures grown by FEBID, where an approximately 80% ratio has been reported.[38]

(ii) Ga $3d^{5/2}$ edge (not shown here): a peak is present at 18.7 ± 0.1 eV, corresponding to metallic gallium.[39]

(iii) Analysis of the Pt $4f^{7/2}$ edge: in Fig. 3(b) we show the Pt 4*f* depth profile. Paying attention to the $4f^{7/2}$ edge, all the spectra can be fitted by one single peak, associated to metallic Pt. This is true in all cases except for the top layer (200 nm), which is much broader, where an extra peak is necessary to fit the spectrum. This extra contribution is lo-

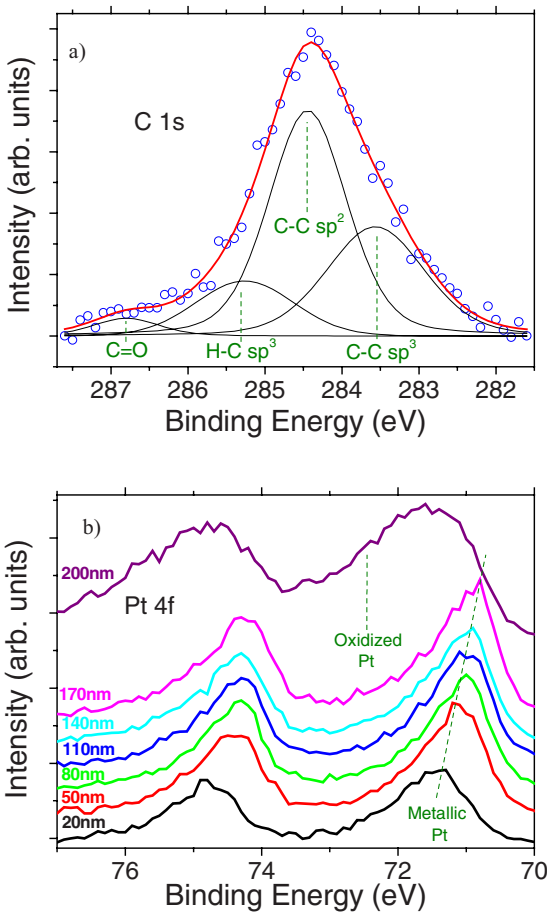

FIG. 3. (Color online) (a) C 1*s* XPS core level for the 170-nm-thick layer (corresponding to a 30 nm in-depth etching). The solid lines are the components in which the spectrum is decomposed. The resulting fit is superimposed on the experimental data (open circles). The energies found for the peaks are associated with C-C sp^3, C-C sp^2, C-H sp^3, and C=O (see text for details). The carbon present in the deposit has approximately 50% sp^2 hybridization through all the deposit thickness. (b) Pt 4*f* core level XPS depth profile. Successive spectra were obtained after a 30 nm argon etching process. The numbers in the figure refer to the remaining sample thickness. The external surface of the deposit presents a broader spectrum than the rest, as a consequence of an extra peak present, associated with platinum oxide or hydroxide (left dashed line). For the rest of surfaces, the spectra can be fitted by only one contribution, associated to metallic platinum. This peak presents a shift toward lower binding energies as the probed layer is increasingly internal (oblique, right dashed line), as well as a decrease in the asymmetry of the Pt 4*f* peak. We correlate this evolution with thickness with a progressive increase in the cluster sizes as the deposit gets thicker.

cated at 72.5 ± 0.1 eV, indicating the presence of oxidized Pt in the external surface, in the form of an oxide or hydroxide form.[37] In the O 1*s* edge, a peak at 531.2 ± 0.1 eV gives account of it. This oxidation seems to be of outstanding relevance for the transport properties of the NWs with small thickness (lower than 50 nm) when exposed to ambient conditions (see Sec. III D).

For the rest of Pt 4*f* spectra, we can see substantial differences with thickness. First, a progressive shift toward higher binding energies (BEs) occurs from the more external part of the deposit (170 nm) to the more internal one (20 nm) (see oblique line). For the 170 nm spectrum, the maximum is located at 70.7 ± 0.1 eV. This BE matches the range typically found at the surface of Pt crystals.[40] For the 20 nm spectrum, the maximum shifts in BE to the value of 71.2 ± 0.1 eV. The second important thickness-dependent feature is associated with the asymmetry of the peaks. The asymmetry in XPS peaks for metallic systems is caused by the screening of the core-hole by low energy electron-hole excitation at the valence band.[31] By fitting the peaks with the line shape proposed by Doniach and Sunjic[30] to describe this effect [Eqs. (1a) and (1b)], we find that whereas the outer surfaces present an asymmetry factor $\alpha = 0.18 \pm 0.04$, matching perfectly with the value for bulk Pt,[31] the more internal surfaces have $\alpha = 0.10 \pm 0.06$. This lower value for the asymmetry is presumably caused by a decrease in the local density of *d* states at the Fermi level.[41,42] The lifetime width of the core hole created by photoemission is almost constant through the entire thickness, $\gamma = 0.56 \pm 0.05$. This value is higher than for bulk Pt, which is typical for small metal clusters.[41,43] The two features found as the deposited thickness increases (enhancement in the degree of asymmetry and shift toward lower BE) would be compatible with an increase in size of the Pt clusters[41,43] with thickness.

C. In situ measurements of the resistance as the NWs are grown

As we explained in Secs. I and II, we have measured the resistance of the NWs as the growth process is performed. In Fig. 4(a) we show how the resistivity (ρ) of a NW evolves as a function of time in a typical experiment. The highest value for ρ corresponds to ~ 1 GΩ in resistance and to ~ 1 kΩ for the lowest value. We have correlated the process time (T_p) with the deposited thickness by doing cross-section inspections of NWs created at different times. Thus, we can also express the results in terms of resistivity, by using the relation as follows:

$$\rho = R \frac{w \times t}{L}. \tag{2}$$

We can see that under these conditions the resistivity of the NWs starts from a value above 10^8 $\mu\Omega$ cm. An abrupt decrease is produced as the thickness increases, lowering its resistivity in 4 orders of magnitude when the thickness reaches 50 nm. From that moment on, ρ decreases slightly, saturating to a constant value of ~ 700 $\mu\Omega$ cm (around 65 times higher than the value for bulk Pt) for $t > 150$ nm. The negligible thickness dependence of ρ for thickness >50 nm was previously evidenced in reference 14. We have not observed an increase in ρ for long T_p as a consequence of the disorder created by ions, such as that reported for W and Pd-FIBID.[19] This procedure has been repeated many times (~ 10), the behavior being the same in all cases. From these experiments, we conclude that the resistivity at room temperature is highly dependent on the NW thickness. This result explains the large diversity of values for ρ_{RT} of FIBID-Pt NWs reported in the literature.[7–18] We must emphasize that

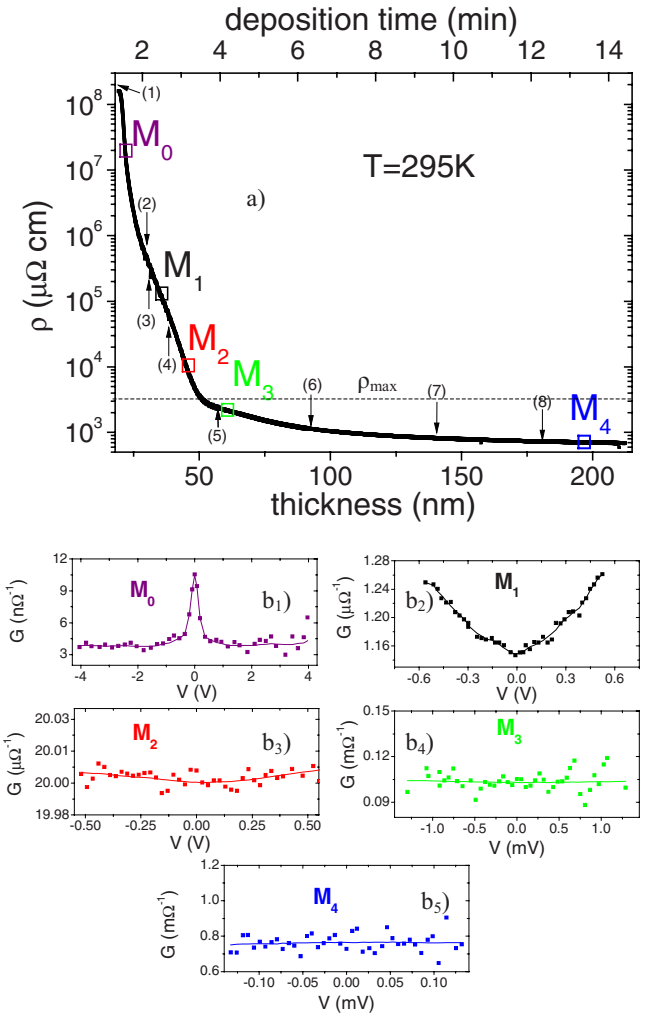

FIG. 4. (Color online) (a) Resistivity as a function of deposition time and thickness for a typical process. The resistivity varies by more than 4 orders of magnitude as a consequence of a change in composition. A thickness of 50 nm marks the transition between a nonmetallic conduction ($t<50$ nm) and metallic one ($t>50$ nm). The resistivity saturates to a constant value for $t>150$ nm, $\rho \approx 700\ \mu\Omega$ cm (about 65 times higher than bulk Pt). The maximum resistivity for metallic conduction in noncrystalline materials (ρ_{max}), as calculated by Mott, is marked. This line separates the insulator NWs from the metallic ones. The numbers in parentheses correspond to different probe currents during the measurements. (1) 5, (2) 10, (3) 30, (4) 100 nA, (5) 5, (6) 3, (7) 5, (8) 10 μA. (b) Differential conductivity versus voltage for samples in different regimes of conduction, marked in the $\rho(t)$ curve [Fig. 4(a)]. $G(V)$ has been obtained by a numerical differentiation of current-versus-voltage curves. In M_0, an exponential decrease in the differential conductance is present. In M_1, a positive tendency for the $G(V)$ curve is observed, being hard to see for M_2. In M_3 and M_4, $G(V)$ is constant (see text for details). The lines are guides to the eyes.

the chosen parameters are of great importance in the particular values of the resistivity for a given thickness since effects such as heating, diffusion, and interaction of the beam with substrate, can differ depending on the conditions. We are not able to reach resistivities as low as the ones reported by Lin *et al.*[9–11] The different precursor gas used for deposition, as it was pointed out in Sec. II C, seems to be the most probable reason for it. The resistivity as a function of thickness crosses the value reported by Mott for the maximum metallic resistivity for a noncrystalline material, $\rho_{max} \approx 3000\ \mu\Omega$ cm (Ref. 22) at ≈ 50 nm [see dashed line in Fig. 4(a)]. Taking into account this criterion, we would roughly expect a nonmetallic conduction for samples with $\rho > \rho_{max}$ and a metallic conduction for $\rho < \rho_{max}$.

To study the nature of the conductivity in deposits having different thickness, we have fabricated several NWs by means of stopping the growth process when a determined value of the resistivity is reached. Hereafter these NWs will be generically referred to as: M_0 ($\sim 10^7\ \mu\Omega$ cm), M_1 ($\sim 10^5\ \mu\Omega$ cm), M_2 ($\sim 10^4\ \mu\Omega$ cm), M_3 ($\sim 2 \times 10^3\ \mu\Omega$ cm), and M_4 ($\sim 700\ \mu\Omega$ cm) [see squares in Fig. 4(a)]. The resistance in all cases is stable under the high vacuum atmosphere once the deposit has stopped. Current versus voltage (I-V) measurements have been performed *in situ*, at room temperature. In Fig. 4(b) we show examples of the differential conductance ($G=dI/dV$, obtained numerically) as a function of voltage. For M_4 [Fig. 4, (b_5)] and M_3 [Fig. 4, (b_4)], I-V is linear (G constant), so a metallic character is inferred. However, for M_2 [Fig. 4, (b_3)], $G(V)$ is slightly parabolic. This result agrees perfectly with Ref. 8, where this behavior is observed for a deposit of $\rho = 3078\ \mu\Omega$ cm. The same nonlinear effect is even much stronger for M_1 [Fig. 4, (b_2)]. A different behavior in $G(V)$ occurs for the most resistive sample, M_0 [Fig. 4, (b_1)], where a peak in the differential conductance is found at low bias, decreasing from $\sim 10\ \text{n}\Omega^{-1}$ to a constant value of 4 $\text{n}\Omega^{-1}$ for voltages higher than 0.5 V. $G(V)$ measurements confirm Mott's criterion for the maximum resistivity for metallic conduction in noncrystalline materials.[22] We discuss in detail the evolution of $G(V)$ with thickness in Secs. III D and IV.

We can understand these strong differences for the electrical transport properties at room temperature taking into account the results obtained in Sec. III A, where a gradient in composition is observed for the NWs as a function of thickness. For NWs thinner than approximately 50 nm, the metal (Pt+Ga) content is lower than 33% (atomic), resulting in resistivity values orders of magnitude higher than those for pure Pt, together with nonlinear features in the I-V curves. For NWs thicker than 50 nm, the metal content is higher than 33%. In this case, the resistivity reaches a minimum value (about 65 times higher than for Pt), and metallic I-V characteristics are observed. A more detailed discussion will be presented in Sec. IV.

D. Temperature dependence of the electrical properties

For a better understanding of the transport mechanisms in the Pt-C NWs, we have measured the thermal dependence of the resistance, as well as I-V curves at different temperatures. We have studied NWs in the representative ranges shown in Sec. III C: M_0–M_4. The first substantial difference between samples is related to the modification of the resistance when the NWs come into contact with ambient atmosphere. For M_4, M_3 and M_2, we did not observe important changes in R, whereas for M_1 the resistance was roughly doubled, and for

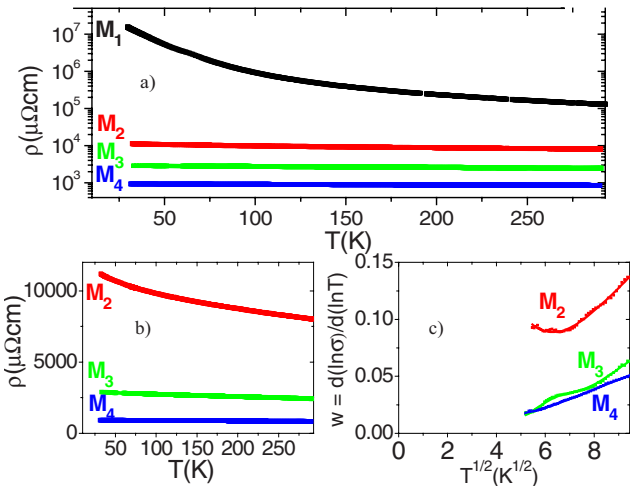

FIG. 5. (Color online) (a): Resistivity as a function of temperature for NWs in four selected regimes of resistivity (note the logarithmic scale). The thermal dependence is radically different depending on the value of ρ at room temperature, indicating a metal-insulator transition as a function of thickness (therefore as a function of composition). (b): $\rho(T)$ curves of M_2, M_3 and M_4 in normal scale, to observe in detail the variations in resistivity for these samples. (c): w (Eq. (3) in text) as a function of $T^{1/2}$. From this analysis, together with the I-V behavior, we deduce that for NWs in the regime of M_3 and M_4 the conduction is metallic, being insulator for the rest of the selected regimes (see text for details).

M_0 it became higher than 1 GΩ. These changes are clearly associated with the oxidation effect for Pt at the top part of the deposits after exposure to ambient conditions (see Sec. III B).

In Fig. 5(a) we show the resistivity versus temperature $[\rho(T)]$ curves for M_1-M_4. We can see a radically different behavior depending on the resistivity at room temperature. In the case of M_1, a highly negative thermal dependence is found, increasing more than 2 orders of magnitude when $T=25$ K ($\mathrm{RRR}=\rho_{\mathrm{RT}}/\rho_{25\ \mathrm{K}}\approx 9\times 10^{-3}$). Nevertheless, in the rest of the samples [see their evolution with temperature in detail in Fig. 5(b)] a low dependence on temperature is found, with RRR slightly lower than 1 ($\approx$0.7 for M_2, $\approx$0.8 for M_3, and $\approx$0.9 for M_4). This is a clear evidence of the important role played by the disorder created by the Ga ion irradiation during the growth, as well as by the inhomogeneous nature of the deposit. We must remark again that a positive thermal coefficient for FIBID-Pt has been shown in literature[9–11] but using a different gas precursor.

We have used the $\rho(T)$ measurements to determine if the NW series presents a MIT with thickness by calculating the variable as follows:

$$w(T)=\frac{d(\ln \rho^{-1})}{d(\ln T)}. \tag{3}$$

The dependence of w upon T is far more sensitive for determining the transition than $\rho(T)$, as has been stressed by Möbius *et al.*[44] $w(T\rightarrow 0)=0$ implies a metallic character of the conduction, whereas either a diverging or finite value for $w(T\rightarrow 0)$ indicates that the sample is an insulator. In our case, the lowest temperature attainable is too high (25 K) for us to apply this criterion strictly. However, in M_2, as shown in Fig. 5(c), $w(T)$ is far from tending to zero, whereas in M_3 and M_4 the behavior of $w(T)$ has this tendency. We could then infer that M_3 and M_4 have metallic conduction, being insulators for the rest. This is in perfect agreement with the results obtained at room temperature (see Sec. III C) and, as will be shown below, with the *I-V* study done as a function of temperature. Therefore, the results support a scenario where the Pt-C NWs grown by FIB present a MIT as a function of thickness (metal/carbon composition). If a low metal content is present, the conduction is attributable to carrier hopping into localized states, whereas a high enough amount of metallic inclusions guarantees that transport will take place by carriers in extended states. This explains the diversity of results found in literature for the dependence of Pt-FIBID resistivity with temperature. It should be noticed that amorphous carbon by itself is well known to present a MIT by tuning the sp^2-sp^3 ratio,[45,46] but in our case the amount of metal present in the deposits is the key parameter for determining the mechanism responsible for conduction.

We have studied in detail $\rho(T)$ in the nonmetallic sample M_1. By fitting the curve using an activation dependence,

$$\rho(T)=\rho_\infty \exp^{(T_0/T)^N}, \tag{4}$$

it is found that the best exponent N is 0.5. Variable-range hopping (VRH) of electrons between localized states, as predicted by Mott and Davis,[22] has the same functional dependence, but with $N=0.25$. Efros and Shklovskii[23] demonstrated that a VRH process when the Coulomb interaction between sites is taken into account (ES-VRH) results in a Coulomb gap, yielding an exponent of 0.5 instead of 0.25. There exists a critical temperature T_c above which Mott-VRH is fulfilled, whereas below T_c, Coulomb interactions become important, and the conduction is by ES-VRH. As discussed in reference 47 for FEBID-Pt nanostructures, a T_c higher than room temperature is expected if reasonable assumptions are made for the values of two unknown quantities in this material: the density of states at the Fermi energy and the dielectric constant. The observed thermal dependence of M_1 suggests that the same arguments are valid in this case. We should also mention that $\rho(T)$ in M_2 also follows this dependence in the low-T regime.

We have also performed *I-V* curves as a function of temperature for all the samples and, as in the case of measurements inside the chamber, differentiated numerically the curves to obtain the differential conductance G. First, for M_4 and M_3, *I-V* curves are linear for all temperatures (not shown here), indicating a metallic character in all the range of T studied. This is not the case for M_2 and M_1. The results are in perfect agreement with the $w(T)$ analysis done before.

In the case of M_2, we show in Fig. 6(a) the normalized conductance G/G_0 versus voltage for selected temperatures, where G_0 is the lowest value for G. The nonlinearity effects increase as T diminishes, reaching 2% $[100(G/G_0-1)]$ at 25 K. We can see that the dependence for this sample is the same as that for the one reported in Ref. 8, where the increase in the differential conductance with voltage was understood in terms of the Glazman-Matveev model[48] for mul-

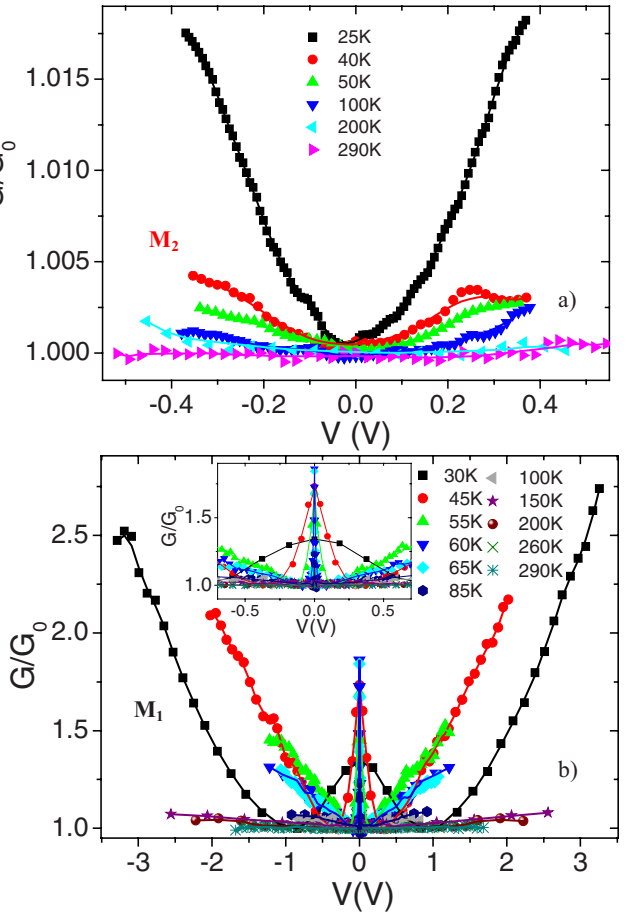

FIG. 6. (Color online) Normalized differential conductance (G/G_0) as a function of voltage for M_2 (a) and M_1 (b). In M_2, a positive differential conductance is observed, increasing the nonlinearity as T is lowered. This dependence is also seen in M_1 at high bias. In M_1, a decrease in the differential conductance is observed for $T<100$ K. The evolution of this phenomenon is shown in detail in the inset of (b).

tistep tunneling occurring between the Pt-Ga nanocrystals embedded in the C-insulator matrix. We will discuss this dependence in Sec. IV.

In Fig. 6(b) we show the normalized conductance for M_1. For temperatures higher than 100 K, the same dependence as in M_2 is exhibited. This sample is much more insulating than M_2, so the nonlinearity at 100 K, for instance, is around 5%. A richer behavior is found for temperatures below 100 K. As can be observed, a peak in $G(V)$ appears at zero bias, as a consequence of a decrease in the conductance for low voltages. It is the same behavior found for the sample M_0 for *in situ* measurements, and we have also reported this behavior in NWs grown by FEBID.[15] For higher V the same nonlinear dependence for $G(V)$ as in sample M_2 is observed. We can see in detail the thermal evolution of the peak in $G(V)$ as a function of temperature in the inset of Fig. 6(b). The height of the peak increases in magnitude as the temperature is lowered, reaching its maximum at 60 K (around 80% at $V=0$). For lower T, the peak becomes broader and smaller in height. On the other hand, the nonlinear effect at high voltages (increase in the differential conductance) is above 150% at 30K. We interpret in detail all these results in Sec. IV.

IV. DISCUSSION

As has been shown in Secs. I–III, the methodology we have used to study the resistivity of Pt-C NWs created by FIB, using an *in situ* measurement of the resistance while the deposit is being performed, has allowed us to determine substantial differences in the electrical transport properties with thickness, i.e., with composition. In this section we discuss the different mechanisms for conduction existing in the NWs and their temperature dependence, which depend on their composition.

The MIT we observe in the NWs as a function of thickness can be understood under the Mott-Anderson theory for noncrystalline materials.[22] Amorphous carbon (a-C) is a disordered semiconductor. The gap when the hybridization is partially sp^2, as we have determined by the XPS analysis, is typically around 1–2.5 eV.[49,50] Because of the intrinsic disorder present in the nanodeposits, band tails appear inside the gap as localized states, with the so-called mobility edge separating localized and nonlocalized states inside the band. If inside a matrix composed by a-C metallic inclusions are introduced in a low percentage (M_0 and M_1), this will mainly result in the incorporation of localized defects within the band gap. The conductivity, especially at low temperatures, will be due to hopping conduction between these defects. As the deposit induced by ions continues (M_2), two effects occur: an increase in disorder favored by the continuous ion irradiation and the incorporation of a higher percentage of metal, as we showed by EDX characterization. The disorder will result in a decrease in the gap by an enlargement of the band tails, resulting in a partial delocalization.[49] Therefore, the hopping will not be only between the impurity states within the gap but also by means of the localized states inside the band, below the mobility edge. An even higher percentage of metallic inclusions will create a continuum of levels, inducing a transition to the metallic regime when the concentration is above the percolation edge (M_3 and M_4). Under this scenario, we can understand the different results reported in literature regarding the transport properties of Pt-C deposits grown by FIB (see Sec. I and Table I). Depending on the carbon concentration, the conduction will be metallic by means of extended states or insulating by a hopping process between localized states.

To understand the mechanisms for conduction in the insulating regime we now focus our discussion on the voltage dependence of the differential conductance for the samples M_0, M_1, and M_2 [Fig. 4 (b_1) and Figs. 6(a) and 6(b)]. We will first interpret the $G(V)$ behavior for the less resistive sample, M_2 [Fig. 6(a)]. As we previously commented, the thermal dependence at low temperatures is associated with an ES-VRH. In this theory, above a critical electric field E^*, the hopping is field dominated, and the conductance is expressed by[51]

$$G = G(0)\exp\left(-\sqrt{\frac{E^*}{E}}\right), \tag{5a}$$

with

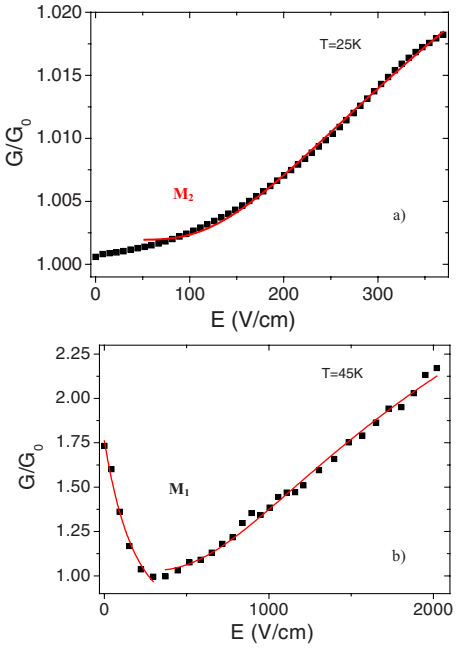

FIG. 7. (Color online) Normalized differential conductance (G/G_0) as a function of the electric field, for M_2 at $T=25$ K (a), and M_1 at $T=45$ K (b). Red solid lines are fits to the experimental data. In (a), the fit is done for $E>50$ V/cm to the ES-VRH model for $E>E^*$ (see Eqs. (5) in text). In (b), the same model is used for the fit if $E>350$ V/cm. If $E<350$ V/cm, the Shklovskii theory to describe an exponential decrease in the hopping conductivity is used (Eq. (6) in text).

$$E^* \approx \frac{1.4e}{4\pi\varepsilon_0\varepsilon\xi_L^2}, \tag{5b}$$

where E is the applied electric field, ε is the dielectric constant, and ξ_L is the localization length. We show in Fig. 7(a) a typical fit performed for M_2 at 25 K. In this case, the data fit quite well to the dependence of Eq. (5a) for fields above 100 V/cm. From Eq. (5b), and assuming a dielectric constant $\varepsilon \approx 4$ for an a-C rich Pt NW,[47,52] we can estimate the localization length as a function of temperature, for $T<125$ K (Fig. 8). Thus, $\xi_L(M_2) \approx 80$ nm for this range of temperatures.

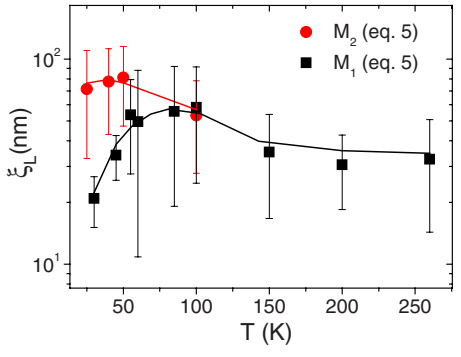

FIG. 8. (Color online) Localization length as a function of temperature derived from the ES-VRH theory (Eqs. (5)) for M_2 and M_1.

The same treatment has been done for the differential conductance of M_1 [Fig. 6(b)], but in this case the ES-VRH dependence in fulfilled in the whole range of temperatures measured. The fit has been done to the part of $G(E)$ where the conductance increases with the electric field. An example for $T=45$ K is shown in Fig. 7(b), where the positive exponential dependence predicted by Eq. (5a) is fitted to the experimental data for fields $E>350$ V/cm. The localization length derived for the fits is shown in Fig. 8. $\xi_L \approx 30-50$ nm for high temperatures, decreasing to a value of about 20 nm for low temperatures. The lowest temperature attained in the setup is quite high (25 K) and could explain why ξ_L is significantly bigger than the size of the metallic crystals in the carbon matrix (around 3 nm) in terms of a thermal effect.[7,9,15]

We should now discuss the origin of the low-bias decrease of the differential conductance found for the most resistive sample in the series (M_0) at room temperature, as well as for M_1 for $T<100$ K. Böttger and Bryksin[24] and Shklovskii and co-workers[25,26] developed analytical models for the hopping conduction in disordered systems under strong electric fields. Those models predict that in certain conditions an exponential decrease in the hopping conductivity with the electric field occurs, even producing a negative differential conductance in certain cases. Experimentally, this was demonstrated in lightly doped and weakly compensated silicon.[26,53] Recently, numerical simulations confirm that this behavior of the conductance as a function of the applied voltage is inherent to the hopping transport in this conduction regime.[54] The theory developed predicts an exponential decrease in the conductance with the electric field in the following form:

$$G(E) \approx G(0)\exp\left(\frac{-eEL_0}{2kT}\right), \tag{6a}$$

with

$$L_0 = \frac{R}{3}\left(\frac{1.74R}{\xi_L}\right)^{0.88}, \tag{6b}$$

where $R=N^{-1/3}$ is the mean interimpurity distance, ξ_L is the localization length, and L_0 is the typical length of the region where the electron gets "trapped." This equation is valid if $eEL_0 \gg kT$. To understand the essence of the effect, let us think of a cluster composed of impurities, responsible for the hopping conduction. In a hopping process at moderate fields, the electron hops from one site to other, opposite to the electric field. In this process, there exists the possibility that the electron arrives at a "dead-end," i.e., an impurity center whose neighboring sites are distant enough to make it energetically unfeasible for the electron to continue its way. If this happens, the electron tries to move in the direction of the field to escape from this "trap" to further continue hopping again opposite to E. However, if the conduction occurs under a strong electric field, some of these backward movements are forbidden. Thus, electrons get trapped in such dead-ends, and consequently the current density decreases with E. For a detailed description of the phenomenon see Refs. 24–26 and 54. We associate the decrease in $G(V)$ found in M_0 and M_1 to this effect, in complete agreement with the previous interpre-

tations done for other ranges of resistivities and fields. As observed experimentally in Figs. 6(b) and 7(b), after the drop in $G(V)$ at low bias, a change to positive slopes appears at even higher fields, which is a direct consequence of the high value of the field, which provides enough energy to overcome the traps in the system, resulting in the dependence of VRH with field described by Eq. (5).[53]

We have used Eq. (6) to fit the experimental $G(E)$ data of M_0 and M_1. In Fig. 7(b), the example for M_1 at 45 K is shown, where the fit is done for $0<E<350$ V/cm. For $T>50$ K, the criterion $eEL_0 \gg kT$ is not fulfilled, resulting in unphysical values for L_0 (≈ 10 μm) and consequently for the localization length (below the nanometer). We therefore center our study on $T<50$ K, where $L_0 \approx 100$ nm. If we assume an impurity concentration similar to that which exists in silicon when the exponential decrease in $G(V)$ is observed, $N \approx 10^{16}$ cm^{-3},[26,53] an estimate of the ξ_L can be made. For low temperatures, $\xi_L \approx 10$ nm. This value approaches the one estimated by the ES-VRH fits for the higher-bias increase in $G(E)$ of around 20 nm. The nonperfect agreement between both values seems logical since assumptions regarding the dielectric constant and the concentration of impurities are done in both models. Nevertheless, the values are on the same order of magnitude, evidencing the consistency of the analysis performed. If we apply the same procedure for M_0 at room temperature, we obtain $L_0 \approx 200$ nm, resulting in a localization length $\xi_L \approx 6$ nm if an impurity concentration $N=5\times10^{15}$ cm^{-3} is assumed.

After having discussed in detail the mechanisms of conduction for high-resistive (low thickness) Pt NWs grown by FIB, we should also mention the coincidence points existing between this kind of deposits and those grown by SEM (FEBID). In spite of the different mechanisms responsible for deposition, the presence of implanted metallic gallium, and the increase in disorder by the interaction of the ions, reports in the literature also show hopping as a possible mechanism of conduction in FEBID-Pt, with nonlinearities similar to those that we find for insulator NWs deposited with FIB.[15,55,56] The previous reports comparing both materials mainly focus on the differences found between low-ρ-FIBID-Pt and FEBID-Pt.[7,15,57] Further work is necessary to study the similarities and differences between both systems.

We would like to stress the high amount of organometallic gas precursors used to deposit nanostructures in FIBID and FEBID.[1,5] The results reported in this work show the crucial importance of the metal-carbon ratio. Besides, the growth parameters are well known to change drastically the composition of these deposits.[1,5,7,14] Up to now, research in this field has focused on creating deposits that are as pure (metallic) as possible, even performing post-treatments to improve the purity of these nanostructures. This study shows the possibility to create with the same setup but changing a specific parameter (in our case it was the thickness, but it could be another: the substrate, overlap, flux of ions, etc.) a nanostructure with a completely different resistance, and therefore conduction mechanism.

We should also point out the importance of the discovery of an exponential decrease in the differential conductance behavior in low-metallic doped carbon grown with a FIB since it constitutes an experimental evidence in a nanometric structure of the validity of the theories developed for hopping conduction in strong fields. The fact that this behavior was previously found in a FEBID Pt-C NW (Ref. 15) indicates that this conduction process naturally appears in Pt-C NWs grown with focused-beam methods.

V. CONCLUSION

We have presented a detailed study of the transport properties of Pt-C NWs grown by focused-ion-beam-induced deposition. By controlling the resistance as the deposit is done, we can see the different regimes for the resistivity existing in this material.

ρ varies over more than 4 orders of magnitude for the first 50 nm deposited, tending to a constant value for higher thickness. The first abrupt change, as EDX and STEM results show, is dominated by a gradient in composition with thickness, with a richer carbon percentage in the first deposited layers, which we interpret to be caused by the varying effective substrate, or by a heating effect. XPS measurements show the important oxidation in the top layer of the deposit, an approximated 50% sp^2 hybridization of carbon, and we speculate that an increase in the cluster size with thickness will occur.

We have deposited NWs in five different regimes of conductivity (five different thicknesses). By studying NW resistivity as a function of temperature, as well as the dependence with voltage on the differential conductivity, we observe a metal-insulator transition in the NWs as a function of thickness (carbon-metal content). This transition is interpreted under the theory of Mott-Anderson for nonmetallic disordered materials. As the NW increases in height, a higher concentration of metal is introduced in the semiconducting carbon matrix. This gives rise to the appearance of impurity levels in the band gap, together with the localization of states in the formed band tails. As the growth continues, the introduction of metal clusters finally results in a delocalization of the electron wave functions, and NWs above 50 nm present metallic conduction.

A thorough study of the transport properties of the insulating samples has been done, concluding that an Efros-Shklovskii-variable-range hopping seems to be the most probable mechanism for conduction. The richest-in-C nanostructures have a peak in the differential conductance at low bias. This result can be interpreted under the theories developed for hopping in weakly compensated semiconductors, where the presence of a strong electric field "traps" the electron, resulting in a decrease in current with bias.

This work explains the discrepancy existing for previous Pt-C nanostructures created by FIB, where in some cases a metallic character was reported, in contrast to others, where insulating conduction was observed. It also gives a counterpoint to the traditional work when growing metal nanostructures by FIB since we demonstrate the possibility to deposit materials with different conduction characteristics, making it, in principle, feasible to fabricate insulator or metal nanowires with the same technique and precursor, just by controlling and changing the growth parameters.

ACKNOWLEDGMENTS

The authors would like to thank Aleksandra Szkudlarek for help in the XPS spectra analysis, J. V. Oboňa for SRIM simulations, and P. Guinea for discussion on the conductance curves. This work was supported by the Spanish Ministry of Science (through Projects No MAT2008-03636-E, No. MAT2005-05565-C02, and No. MAT2008-06567-C02, including FEDER funding), and the Aragon Regional Government.

*Corresponding author; deteresa@unizar.es

[1] I. Utke, P. Hoffmann, and J. Melngailis, J. Vac. Sci. Technol. B **26** (4), 1197 (2008).
[2] L. A. Giannuzzi and F. A. Stevie, *Introduction to Focused Ion Beams* (Springer, Boston, 2005).
[3] A. D. Dubner, A. Wagner, J. Melngailis, and C. V. Thompson, J. Appl. Phys. **70**, 665 (1991).
[4] S. K. Matsui, J. Vac. Sci. Technol. B **18**, 3181 (2000).
[5] W. F. van Dorp and C. W. Hagen, J. Appl. Phys. **104**, 081301 (2008).
[6] A. Botman, J. J. Mulders, R. Weemaes, and S. Mentik, Nanotechnology **17**, 3779 (2006).
[7] R. M. Langford, T.-X. Wang, and D. Ozkaya, Microelectron. Eng. **84**, 784 (2007).
[8] L. Peñate-Quesada, J. Mitra, and P. Dawson, Nanotechnology **18**, 215203 (2007).
[9] J.-F. Lin, J. P. Bird, L. Rotkina, and P. A. Bennett, Appl. Phys. Lett. **82**, 802 (2003).
[10] J.-F. Lin, J. P. Bird, L. Rotkina, A. Sergeev, and V. Mitin, Appl. Phys. Lett. **84**, 3828 (2004).
[11] J.-F. Lin, L. Rotkina, J. P. Bird, A. Sergeev, and V. Mitin, Proc. 2nd Quantum Transport Nano-Hana International Workshop, IPAP Conf. Ser. **5**, 17 (2004).
[12] T. Tao, J. Ro, and J. Melngailis, J. Vac. Sci. Technol. B **8**, 1826 (1990).
[13] J. Puretz and L. W. Sawson, J. Vac. Sci. Technol. B **10**, 2695 (1992).
[14] K. A. Telari, B. R. Rogers, H. Fang, L. Shen, R. A. Weller, and D. N. Braski, J. Vac. Sci. Technol. B **20**, 590 (2002).
[15] J. M. De Teresa, R. Córdoba, A. Fernández-Pacheco, O. Montero, P. Strichovanec, M. R. Ibarra, J. Nanomater. **2009**, 936863 (2009).
[16] Y. Tsukatani, N. Yamasaki, K. Murakami, F. Wakaya, and M. Takai, Jpn. J. Appl. Phys., Part 1 **44**, 5683 (2005).
[17] K. Dovidenko, J. Rullan, R. Moore, K. A. Dunn, R. E. Geer, and F. Heuchling, *Three-Dimensional Nanoengineered Assemblies*, MRS Symposia Proceedings No. 739, (Materials Research Society, Pittsburgh, 2003), p. H7.7.1.
[18] G. D Marzi, D. Iacopino, A. J. Quinn, and G. Redmond, J. Appl. Phys. **96**, 3458 (2004).
[19] D. Spoddig, K. Schindler, P. Rodiger, J. Barzola-Quiquia, K. Fritsch, H. Mulders, and P. Esquinazi, Nanotechnology **18**, 495202 (2007).
[20] A. Fernández-Pacheco, J. M. De Teresa, R. Córdoba, and M. R. Ibarra, Nanotechnology **19**, 415302 (2008).
[21] M. Prestigiacomo, L. Roussel, A. Houël, P. Sudraud, F. Bedu, D. Tonneau, V. Safarov, and H. Dallaporta, Microelectron. Eng. **76**, 175 (2004).
[22] N. F. Mott and E. A. Davis, *Electronic Processes in Non-Crystalline Materials* (Oxford University Press, New York, 1971).
[23] A. L. Efros and B. I. Shklovskii, J. Phys. C **8**, L49 (1975).
[24] H. Böttger and V. V. Bryksin, Phys. Status Solidi B **96**, 219 (1979).
[25] N. Van Lien and B. I. Shklovskii, Solid State Commun. **38**, 99 (1981).
[26] D. I. Aladashvili, Z. A. Adamia, K. G. Lavdovskii, E. I. Levin, and B. I. Shklovskii, Sov. Phys. JETP **47**, 466 (1988).
[27] T. Schwamb, B. R. Burg, N. C. Schirmer, and D. Poulikakos, Appl. Phys. Lett. **92**, 243106 (2008).
[28] F. Hernandez-Ramirez, A. Tarancon, O. Casals, E. Pellicer, J. Rodriguez, A. Romano-Rodriguez, J. R. Morante, S. Barth, and S. Mathur, Phys. Rev. B **76**, 085429 (2007).
[29] G. Boero, I. Utke, T. Bret, N. Quack, M. Todorova, S. Mouaziz, P. Kejik, J. Brugger, R. S. Popovic, and P. Hoffmann, Appl. Phys. Lett. **86**, 042503 (2005).
[30] S. Doniach and M. Sunjic, J. Phys. C **3**, 285 (1970).
[31] S. Hüfner and G. K. Wertheim, Phys. Rev. B **11**, 678 (1975).
[32] K. Ohya and T. Ishitani, Appl. Surf. Sci. **237**, 606 (2004).
[33] SRIM is a group of programs which calculate the stopping and range of ions into matter using an ion-atom collisions treatment. The simulator is available in http://www.srim.org/#SRIM.
[34] I. Utke, J. Michler, P. Gasser, C. Santschi, D. Laub, M. Cantoni, P. A. Buffat, C. Jiao, and P. Hoffmann, Adv. Eng. Mater. **7**, 323 (2005).
[35] S. Takabayashi, K. Okamoto, K. Shimada, K. Motomitsu, H. Motoyama, T. Nakatani, H. Sakaue, H. Suzuki, and T. Takahagi, Jpn. J. Appl. Phys. **47**, 3376 (2008).
[36] J. Díaz, G. Paolicelli, S. Ferrer, and F. Comin, Phys. Rev. B **54**, 8064 (1996).
[37] V. Alderucci, L. Pino, P. L. Antonucci, W. Roh, J. Cho, H. Kim, D. L. Cocke, and V. Antonucci, Mater. Chem. Phys. **41**, 9 (1995).
[38] S. Frabboni, G. C. Gazzadi, and A. Spessot, Physica E **37**, 265 (2007).
[39] C. D. Wagner, W. M. Riggs, L. E. Davis, J. F. Moulder, and G. E. Muilenberg, *Handbook of X-Ray Photoelectron Spectroscopy* (Perkin-Elmer Corporation, Eden Prairie, MN, 1979).
[40] R. C. Baetzold, G. Apai, E. Shustorovich, and R. Jaeger, Phys. Rev. B **26**, 4022 (1982).
[41] T. T. P. Cheung, Surf. Sci. **140**, 151 (1984).
[42] A. Y. Stakheev, Y. M. Shulga, N. A. Gaidai, N. S. Telegina, O. P. Tkachenko, L. M. Kustov, and K. M. Minachev, Mendeleev Commun. **11**, 186 (2001).
[43] K. Fauth, N. Schneider, M. HeßIer, and G. Schütz, Eur. Phys. J. D **29**, 57 (2004).
[44] A. Mobius, C. Frenzel, R. Thielsch, R. Rosenbaum, C. J. Adkins, M. Schreiber, H. D. Bauer, R. Grotzschel, V. Hoffmann, T. Krieg, N. Matz, H. Vinzelberg, and M. Witcomb, Phys. Rev. B **60**, 14209 (1999).

[45] V. Prasad, Solid State Commun. **145**, 186 (2008).
[46] S. Bhattacharyya and S. R. P. Silva, Thin Solid Films **482**, 94 (2005).
[47] Z.-M. Liao, J. Xun, and D.-P. Yu, Phys. Lett. A **345**, 386 (2005).
[48] L. I. Glazman and K. A. Matveev, Sov. Phys. JETP **67**, 1276 (1988).
[49] R. U. A. Khan, J. D. Carey, S. R. P. Silva, B. J. Jones, and R. C. Barklie, Phys. Rev. B **63**, 121201(R) (2001).
[50] J. Robertson, Mater. Sci. Eng. R. **37**, 129 (2002).
[51] D. Yu, C. Wang, B. L. Wehrenberg, and P. Guyot-Sionnest, Phys. Rev. Lett. **92**, 216802 (2004).
[52] A. Grill, Diamond Relat. Mater. **10**, 234 (2001).
[53] A. P. Mel'nikov, Yu A. Gurvich, L. N. Shestakov, and E. M. Gershenzon, JETP Lett. **73**, 50 (2001).
[54] A. V. Nenashev, F. Jansson, S. D. Baranovskii, R. Österbacka, A. V. Dvurechenskii, and F. Gebhard, Phys. Rev. B **78**, 165207 (2008).
[55] F. Wakaya, T. Tsukatani, N. Yamasaki, K. Murakami, S. Abo, and M. Takai, J. Phys.: Conf. Ser. **38**, 120 (2006).
[56] J. Fransson, J.-F. Lin, L. Rotkina, J. P. Bird, and P. A. Bennett, Phys. Rev. B **72**, 113411 (2005).
[57] S. Lipp, L. Frey, C. Lehrer, E. Demm, S. Pauthner, and H. Ryssel, Microelectron. Reliab. **36**, 1779 (1996).